RESEARCH ARTICLE
SOLID EARTH: EXPLORATION GEOPHYSICS

Earth and Planetary Physics
6: 385–398, 2022
doi: 10.26464/epp2022039

Application of active-source surface waves in urban underground space detection: A case study of Rongcheng County, Hebei, China

GuangWen Wang[1,2], HaiYan Wang[1,2*], HongQiang Li[3], ZhanWu Lu[1,2], WenHui Li[1,2], and TaiRan Xu[4]

[1]Lithosphere Center, Institute of Geology, Chinese Academy of Geological Sciences, Beijing 100037, China;

[2]Deep-Earth Dynamics Key Laboratory of the Ministry of Natural Resources, Beijing 100037, China;

[3]Chinese Academy of Geological Sciences, Beijing 100037, China;

[4]China Earthquake Network Center, Beijing 100045, China

Key Points:

- The shallow S-wave velocity structure of three survey lines around Rongcheng County, Hebei was obtained by multi-channel surface wave imaging method.
- The S-wave velocity structure corresponds well with the logging results, showing the velocity characteristics of different stratums.
- The predominant period and equivalent shear wave velocity (V_{Se}) show the site characteristics of thestudy area.

Citation: Wang, G. W., Wang, H. Y., Li, H. Q., Lu, Z. W., Li, W. H., and Xu, T. R. (2022). Application of active-source surface waves in urban underground space detection: A case study of Rongcheng County, Hebei, China. *Earth Planet. Phys.*, *6*(4), 385–398. http://doi.org/10.26464/epp2022039

Abstract: Active-source surface wave exploration is advantageous because it has high imaging accuracy, is not affected by high-speed layers, and has a low cost; thus, it has unique advantages for investigating shallow surface structures. For the development and utilization of urban underground space, two parameters in the shallow surface are important, namely, the shear wave velocity (V_S) and the predominant period of the site, which determine the elevation and aseismic grade of the building design. The traditional method is mainly to obtain the two above-mentioned parameters through testing and measuring drilling samples. However, this method is extremely expensive and time consuming. Therefore, in this research, we used the multichannel surface wave acquisition method to extract the fundamental dispersion curve of single-shot data by using the phase shift method and obtain the V_S characteristics in the uppermost 40 m by inversion. We arrived at the following two conclusions based on the V_S profile. First, the study area can be roughly divided into five layers, among which the layers 0–8 m, 14–20 m, and 20–30 m are low-velocity layers, corresponding to miscellaneous fill, a water-bearing sand layer, and a sand layer; therefore, the V_S is relatively low. In contrast, the layers at 8–14 m and 30–40 m are high-velocity layers that are mainly composed of clay, with a relatively better compactness and relatively high V_S values. In addition, a low-speed anomaly appears abruptly in the high-speed area at 20–40 m. This anomaly, when combined with geological data, suggests that it is an ancient river channel. Second, from the V_S value, the V_{Se} (equivalent shear wave velocity) was calculated. The construction site soil was categorized as class III, with good conditions for engineering geology. In addition, we calculated the predominant period of the site to be 0.56–0.77 s based on the V_S. Therefore, in the overall structural design of the foundation engineering, the natural vibration period of the structure should be strictly controlled to avoid the predominant period of the site.

Keywords: Jizhong depression; surface wave exploration; shallow structure; site category; predominant period

1. Introduction

The surface and shallow subsurface support various human activities and construction engineering projects. Therefore, the development and utilization of underground space are very important to human activities. The shear wave velocity (V_S) is one of the key seismological parameters of the shallow subsurface (Fazelabdolabadi and Golestan, 2020; Kamel and Badreddine, 2020; Pan H and Jiang X, 2020). It is also an important reference for the design and construction engineering of some projects and can provide a basis for the division of seismic areas. Therefore, obtaining an accurate V_S in the shallow subsurface has long been an important research direction for geophysicists (Xia JH et al., 2015; Yin XF et al., 2018). At present, the V_S and the predominant period of a site are mainly obtained through drilling sampling and test determination, which is an extremely expensive and time-consuming process (Hua WY et al., 2002; Cao LH et al., 2012; Zhang W et al., 2013). Compared with drilling and other geophysical exploration methods, active-source surface wave exploration has the advantages of a deeper detection range, a lower cost, and greater accuracy, and it is not affected by the high-velocity layers (Du ZT et al., 1999; Cao X et al., 2015; Cai W et al., 2017, 2018).

Correspondence to: H. Y. Wang, hyanwhy@126.com
Received 02 MAR 2022; Accepted 17 MAY 2022.
Accepted article online 28 JUN 2022.

Our study area is located in Rongcheng County, Hebei Province, China. At present, some geological investigations have been carried out around Rongcheng County, including the following:

(1) *Geothermal investigations*: A deep geothermal geological model was constructed to explain the deep heat source mechanism of the Rongcheng geothermal field (Wang K et al., 2021). Through borehole measurements, the temperature range and burial depth of geothermal water around Rongcheng have been determined (Ma F et al., 2021).

(2) *Hydrogeological investigations*: Prior studies have identified the transformational relationship between surface water and groundwater in the Baiyangdian Wetland (Wang YS et al., 2021) and have obtained the location and width of an ancient river channel (Zhang J et al., 2018).

(3) *Investigations of active faults*: One study has revealed the characteristics of hidden faults around Rongcheng (Shang SJ et al., 2019). Using the *in situ* stress measurement method and deep-hole hydraulic fracturing method, Fan YL et al. (2020) have estimated that these concealed active faults will not slide and are relatively stable.

(4) *Engineering environmental geological investigation*: In a prior study, Han B et al. (2020) obtained the physical and mechanical properties of rock and soil in different engineering geological layers by using borehole core data and conducting physical experiments. They also discussed the possible engineering and environmental geological problems and environmental geological effects associated with the development and utilization of underground space.

(5) *Geophysical exploration*: The spatial characteristics within 600 m underground were established by Ma Y et al. (2020) based on shallow reflection exploration, the microtremor survey method, and the high-density electrical method.

The research described above introduces the underground structural characteristics and geophysical properties of Rongcheng County and its surrounding areas from different perspectives. However, it lacks two important parameters of engineering mechanics, the predominant period and the equivalent shear wave velocity (V_{Se}), as well as high-precision characteristics within the uppermost 40 m. Therefore, in this study, we attempted to fill these gaps.

In this work, active-source surface wave exploration technology was used to extract the surface wave signal from a single-shot record, generate and extract the dispersion curve by the phase shift method, and adopt global optimization inversion method. On the basis of the V_S profile, two conclusions were obtained. First, the V_S profile within 40 m was divided into five layers. The layers 0–8 m, 14–20 m, and 20–30 m are low-velocity layers, corresponding to miscellaneous fill, a water-bearing sand layer, and a sand layer, respectively. Layers 8–14 m and 30–40 m are high-velocity layers, mainly composed of clay, with relatively better compactness and relatively high V_S. Second, we calculated the predominant period of the site and the V_{Se} by using the V_S profile. The site of the study area was categorized as class III, with better conditions for engineering geology. In addition, the calculated predominant period of the site ranged from 0.56 to 0.77 s. Therefore, this range should be avoided when constructing the foundation engineering.

2. Geological Background

The Jizhong Depression is located in the northern North China Plain and in the western margin of the rift basin of Bohai Bay. The study area is located at the periphery of the Rong City uplift in the Jizhong Depression, with a relatively flat terrain, and the altitude is generally between 5 and 26 m (He P et al., 2014). The stratum is stable and suitable for construction engineering. According to the depositional age, rock characteristics, and soil type, the study area can be broadly divided into Holocene, upper Pleistocene, and middle Pleistocene strata. The soil types are mainly silty clay, clay, medium sand, and silty sand (Figure 1; Han B et al., 2020). The Holocene silty clay and clay have a moderate bearing capacity, and compression deformation can occur when the load exceeds 130 kPa. In the upper Pleistocene strata, the silty sand and medium sand have low compressibility and a high bearing capacity, so they can be used as the bearing layer of pile foundations. In the middle and lower strata of the Holocene, quicksand and liquefaction of the sand and soil can easily occur during construction. The muddy clay in the lacustrine facies around Baiyangdian has high plasticity and a poor bearing capacity, so these strata cannot be used as the bearing layer in foundation design. During the flood season, when the water level is high, poorly constructed foundations and foundations constructed in areas with poor geological conditions often undergo damage, such as seepage and gushing pipes (Hao AB et al., 2018; Ma Z et al., 2019; Han B et al., 2020). Therefore, it is necessary to study the near-surface structure before designing the infrastructure and continuing urban construction.

3. Data Processing and Analysis

3.1 Data Acquisition

In 2018, we adopted the multichannel analysis of surface waves technique, using the one-sided 99-channel receiving mode of a SmartSolo node seismometer, to complete the original surface wave data acquisition in the central sedimentary plain of the Jizhong Depression. To fully receive the surface wave signal, we tested the number of receiving channels of the observation system. Compared with the traditional 12-, 24-, 36-, and 48-channel acquisition methods (Song YY et al., 1989; Park et al., 1999), the 99-channel acquisition could more fully receive the low-frequency signal of surface waves. As shown in Figure 3, in the dispersion diagram of channels 12, 24, 36, and 48, the effective low-frequency signals were 17.5, 15, 12.5, and 7.5 Hz, respectively. However, the low-frequency signal of 5 Hz could be obtained by 99-channel reception. Compared with the traditional acquisition method, the low-frequency signal could be obtained, and the inversion depth was deeper. In addition, compared with the traditional wired detector (Figure 2b), the nodal seismograph used in this study could complete the mobile acquisition by arranging the first few geophones in the acquisition process, greatly saving on acquisition time. The acquisition parameters were set as follows: the receiver spacing was 2 m, the shot spacing was 8 m, the mini-

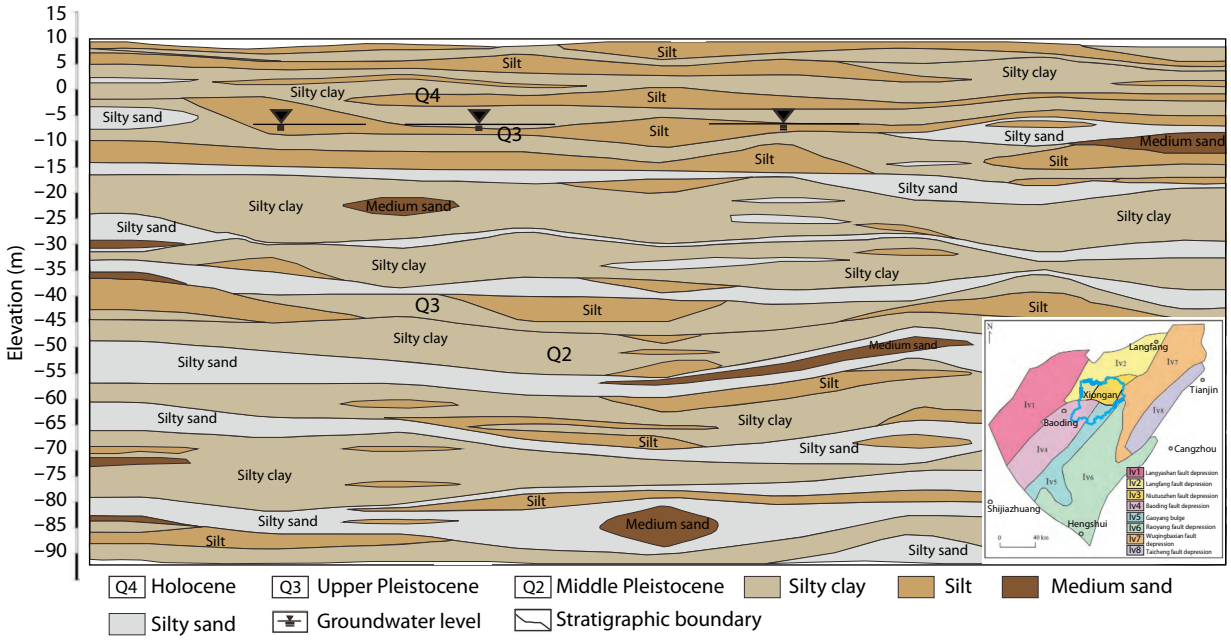

Figure 1. Characteristics of subsurface rock and soil stratification in Rongcheng County (Han B et al., 2020).

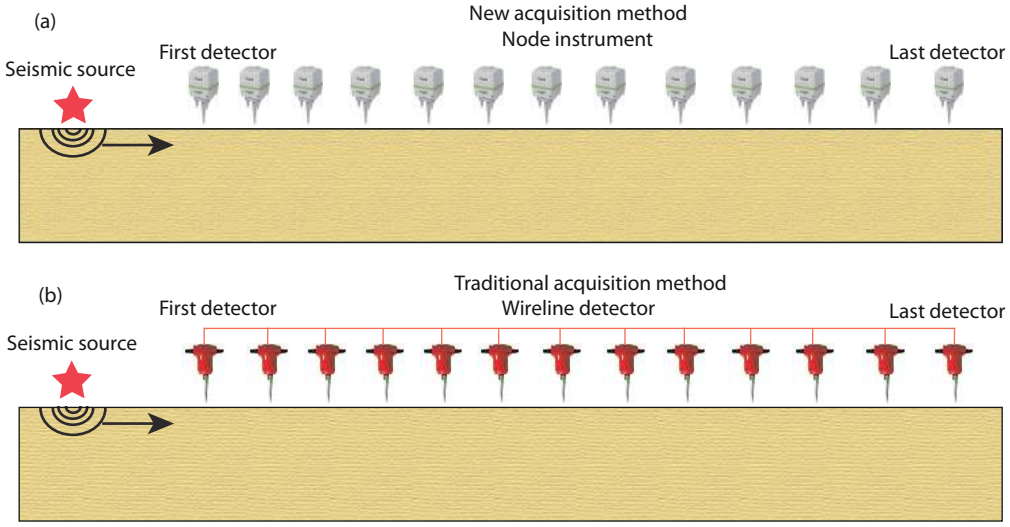

Figure 2. Different geophone acquisition methods.

mum offset was 2 m, the sample interval was 1 ms, and the data recording length was 6 s. We acquired a total of three lines of data (Figure 4): line 1 (L1, red) had an east–west strike and was 4.0 km in length, line 2 (L2, green) had an east–west strike and was approximately 1.0 km in length, and line 3 (L3, blue) had a north–south strike and was 2.5 km in length. The specific acquisition parameters are shown in Table 1.

3.2 Data Analysis

We selected a single shot from different positions along L1 (Figure 5), corresponding to points 1, 100, 200, and 300, for analysis of the amplitude spectrum. By comparing different single shots, we found that the frequency was within 0–50 Hz and that the amplitude was relatively large. After 50 Hz, the amplitude value attenuated rapidly, and these signals corresponded to high-frequency interference waves (Figure 6). Therefore, before surface wave extraction of a dispersion curve, it was necessary to filter out the high-frequency interference and retain effective signals between 0 and 50 Hz.

3.3 Data Processing

In this study, we mainly used the active-source surface wave data processing method. The V_S was obtained by collecting surface wave signals, extracting the dispersion curve, and inverting (Dal Moro et al., 2007; Jin C et al., 2016; Aleardi et al., 2020; Lei T et al., 2020; Shao XH et al., 2022). The V_S was divided into strata according to geological and logging data, and the predominant period and V_{Se} of the site were calculated according to an empirical formula to evaluate the site type. The specific technical route is shown in Figure 7.

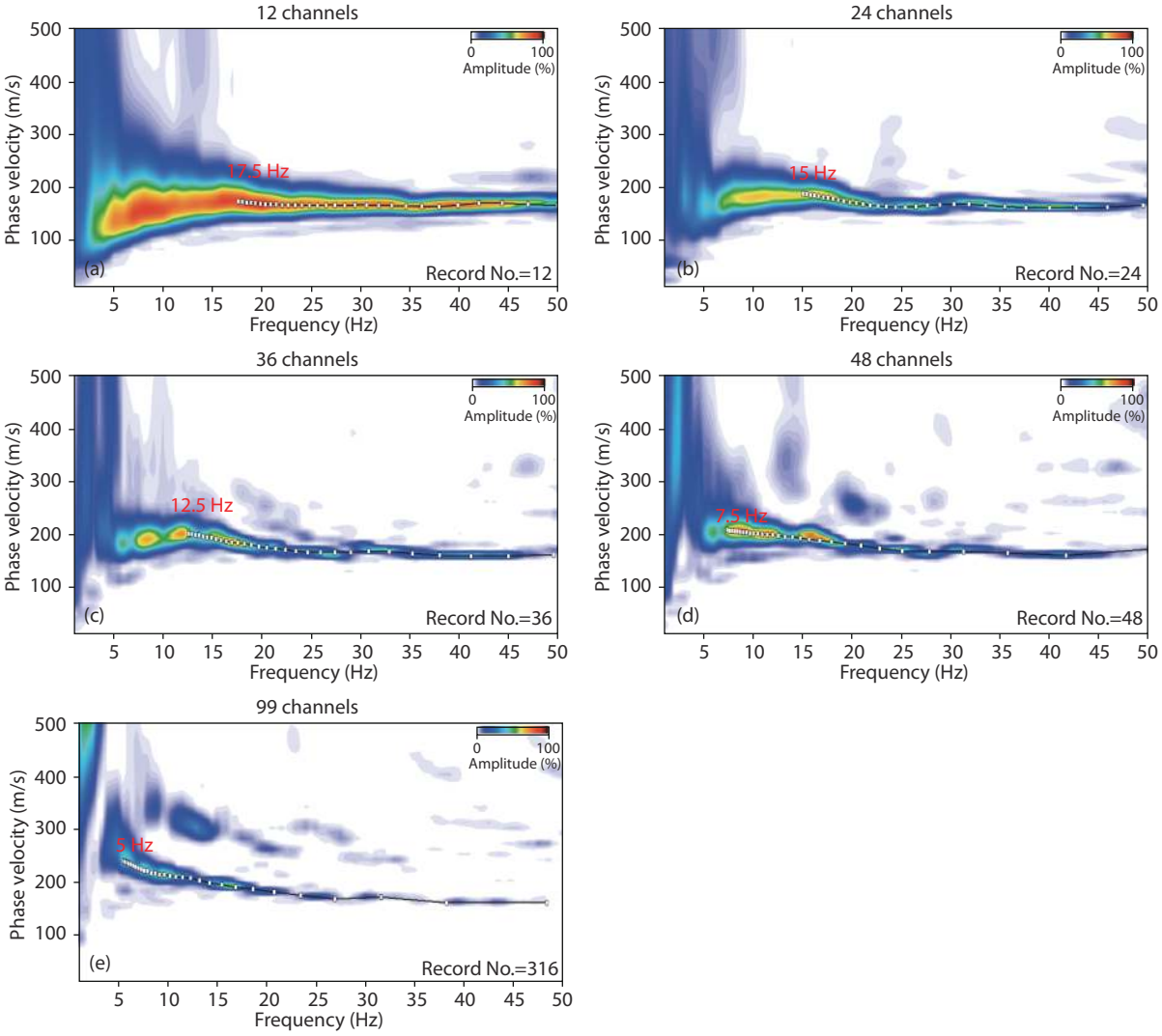

Figure 3. Dispersion energy diagram of different receiver channels.

3.3.1 Dispersion Curve Extraction

Obtaining the dispersion curve is one of the key steps in surface wave data processing. First, we used ParkSEIS software to conduct a frequency spectrum analysis of the single-shot data, filter out the high-frequency interference, and retain the 0–50 Hz effective surface wave signals. The single shot in the time–space domain was then transformed into the frequency–velocity domain by the phase-shift method (Park et al., 1999). The surface wave record in the frequency domain was expressed as the product of amplitude and phase and was normalized to form a dispersion energy diagram (Figure 8). It can be seen from the dispersion energy diagram that the continuity of the fundamental dispersion curve was superior. The frequency range was 5–40 Hz, and the phase velocity was 100–300 m/s. Finally, we used ParkSEIS software to pick up the fundamental dispersion curve automatically by setting the picking range. To improve the imaging accuracy in the process of picking up the dispersion curve, we removed data with a low signal-to-noise ratio and retained only data with a high signal-to-noise ratio, which increased the credibility of the results.

3.3.2 Initial Model Establishment

The initial model included many parameters, such as the formation thickness, density, V_S, and V_P (which is compressional wave velocity; Andajani et al., 2019). For the n-layer model, multiple parameters needed to be inverted. If all the model parameters were inverted as independent variables, the inversion calculation would be very large, which would create difficulties in the calculation. It was found through experiments that the V_S and the thickness of the stratum had a great influence on the accuracy of the inversion results, whereas the density and V_P had a small influence (Xia JH et al., 2015). Therefore, we adopted a simplified method, and the initial model considered only the layer thickness and V_S in the inversion. Such a simplified method is currently widely used in surface wave inversion. Although certain inversion effects can be obtained with this approach, parameters such as the layer number, layer thickness, and layer velocity must constantly be corrected during the inversion process.

We selected part of the dispersion curves for testing and analysis and found that the inversion depth of the dispersion curves of the three lines was within 40 m from the surface. After combining data from the engineering geology and logging of the research study area (Figure 1; Han B et al., 2020), the inversion of the layers within 40 m from the surface was divided into seven layers. By

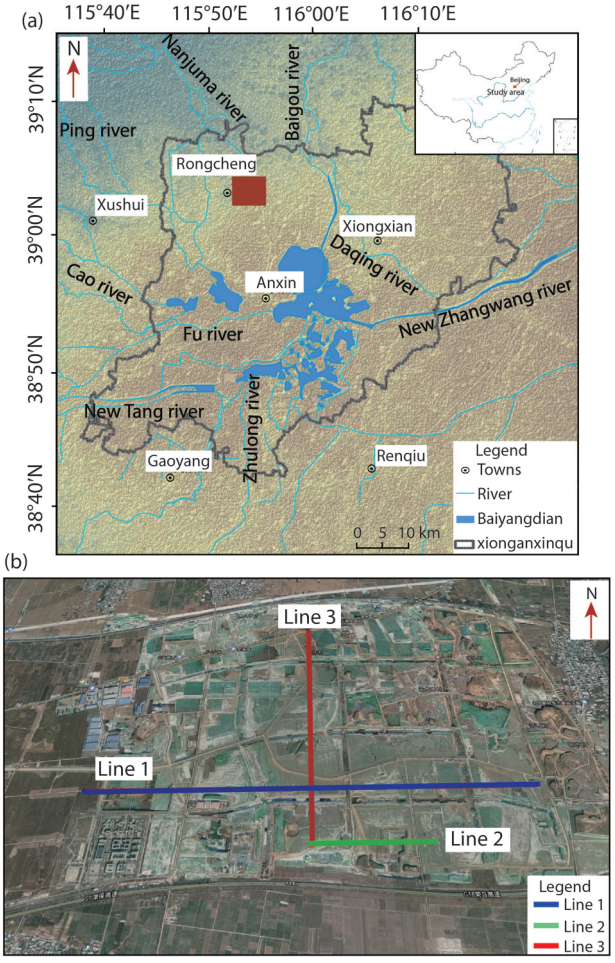

Figure 4. Line position: (a) location of Xiong'anxinqu; (b) map of the surrounding area of Rongcheng County.

comparing the degree of fit of the measured curve and the forward curve, we concluded that the model was suitable when the one-dimensional inversion error of all the dispersion curves was within a range of 5%. The initial model was determined by repeated comparison tests (Table 2).

3.3.3 Inversion of the Dispersion Curve

On the basis of the initial model, a global optimization inversion method was adopted to obtain V_S for the fundamental-order dispersion curve. In Figure 9, the blue line is the V_S by inversion, the blue points of the dispersion curve were obtained through forward modeling based on the theoretical model, and the red points were the picked dispersion curve. The inversion results showed that the selected dispersion curve corresponded well to the dispersion curve obtained by forward modeling based on the theoretical model. The degree of fit was high, especially in the low-frequency area. However, in the high-frequency area, a certain error was present because of noise in the raw data, so the extraction of the dispersion curve and the theoretical model of the dispersion curve were inconsistent. The one-dimensional inversion results at point 10 in Figure 9 show that the velocity of the first layer increased successively to the fifth layer and that the velocity of the sixth layer began to decrease. The results of points 36 and 56 show a low-velocity layer at approximately 30–40 m, whereas a low-velocity layer may also be present at 10–18 m.

Table 1. Data acquisition parameters.

Acquisition parameter	Line 1	Line 2	Line 3
Source	Dynamite	Dynamite	Dynamite
Shot spacing (m)	8	8	8
Receiver spacing (m)	2	2	2
Minimum offset (m)	2	2	2
Sample interval (ms)	1	1	1
Record length (s)	6	6	6
Heavy hammer quality (kg)	90	90	90
Profile length (km)	4.0	1.0	2.5
Shot number	508	116	289

3.3.4 Reliability Analysis

To verify the reliability of the results, we examined two logging curves for L1 for analysis and verification (Figure 10). The logging curves had four parameters: gamma ray, apparent resistivity, natural potential, and interval transit time. Increases in the gamma ray value and apparent resistivity indicate an increase in shaliness and a decrease in fluid content. A high natural potential value indicates weak permeability. A high interval transit time indicates a high porosity and poor compactness. Therefore, we reached the following conclusions from the logging curves of the two wells:

(1) *GB032 logging*: At 12 to 32 m, the gamma ray value, apparent resistivity value, and natural potential value are high, and the interval transit time is low. These data suggest that the sedimentary strata are shaly and have a low porosity, relatively weak permeability, and good compactness. At 32 to 40 m, the gamma ray value, apparent resistivity value, and natural potential value are low, and the interval transit time is high. Thus, the shaliness is relatively low, the porosity is high, the permeability is high, and the compactness is poor. Hence, the sediment from 12 to 32 m is mainly a silty layer with good compactness and a high degree of shaliness, whereas that from 32 to 40 m is mainly a water-bearing sand layer with strong permeability and little shaliness.

(2) *GB034 logging*: From 12 to 20 m, the gamma ray value and the natural potential value are relatively low, and the apparent resistivity has a minimum value, indicating that the degree of shaliness is low, the porosity is high, the permeability is high, and an underground water layer is present. From 20 to 25 m, the gamma ray and natural potential values increase, and the apparent resistivity has a maximum value, indicating an increase in shaliness, a decrease in porosity, and a decrease in permeability. From 25 to 40 m, the gamma ray jumps abnormally, the apparent resistivity continues to decrease, and the natural potential increases. This result suggests that silt and sand are interbedded in this layer, the shaliness changes greatly with depth, and the porosity also changes greatly. Therefore, we suspected that a water-bearing silty sand layer is present from 12 to 20 m and that it has a high permeability. From 20 to 25 m, the silty clay has good compactness. From 25 to 40 m, the sediment is mainly silt, and the sand

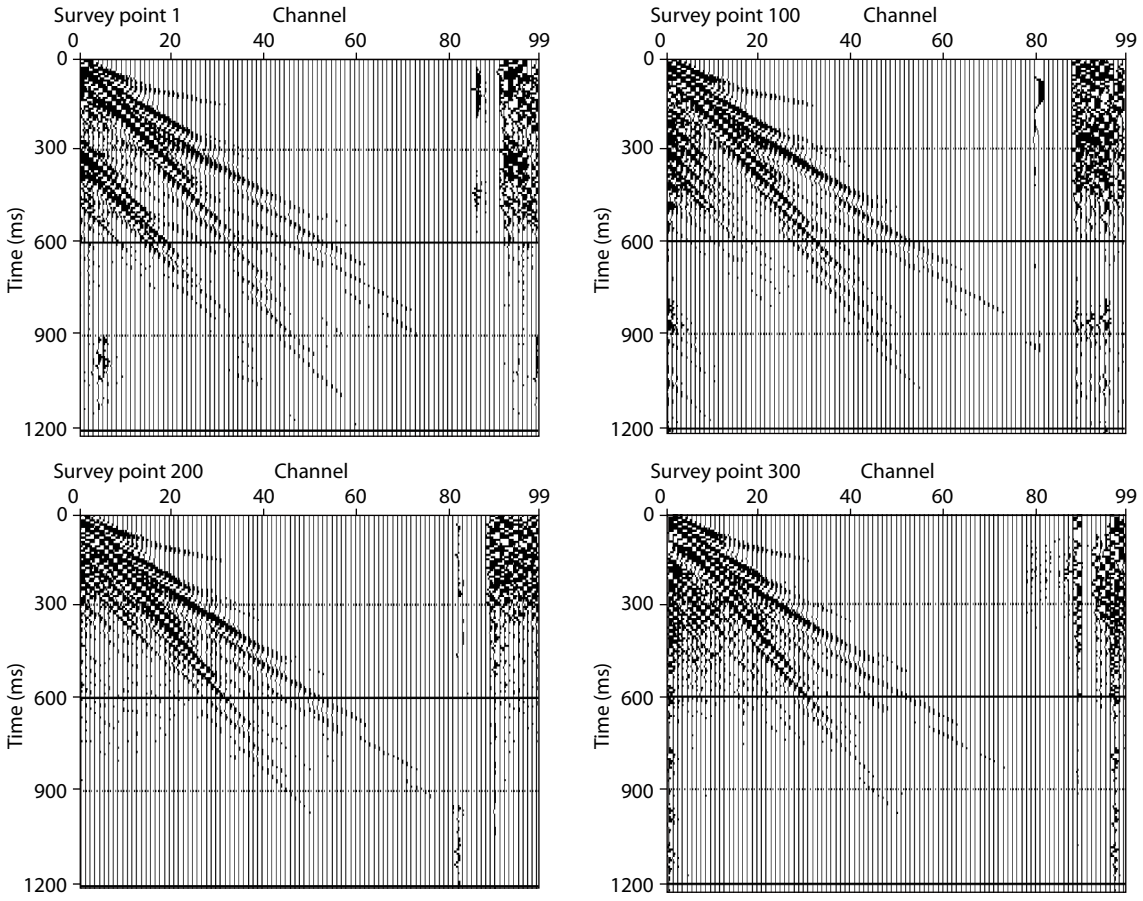

Figure 5. Original single-shot records (points 1, 100, 200, and 300 are surveying points with an equal interval spacing along line 1).

content may be high locally.

We projected the logging stratification results onto the V_S profile of L1, and the corresponding results were superior. At GB032, the silty sand and silty soil in the lowest layer is an aquifer, which corresponds to the low-velocity zone between 30 and 40 m. The silt layer spans from approximately 12 to 34 m and corresponds to the low-velocity region, which may be an ancient channel. At GB034, the logging results showed a silty sand layer with a high water content, which corresponds to the low-velocity layer in the inversion results. Because silty clay has good compacting properties and is a natural aquiclude, the V_S is high. The bottom layer of silt corresponds to the high-velocity layer of the inversion results.

4. Site Evaluation

4.1 Site Classification

At present, according to survey specifications in engineering geology, the site soil should be within a depth of 30 m, and the V_S and sedimentary layer thickness should determine the site type. These specifications have an important impact on the stability and safety of the engineering facilities (Pasquet et al., 2015; Sairam et al., 2019; Chimoto and Yamanaka, 2019). Several building codes have adopted the V_{Se} (*which refers to the weighted average velocity of the S-wave wihtin 30 m under ground*) as the preferred site parameter for common engineering applications and ground motion prediction studies (Boore et al., 1994; Rastogi et al., 2011; Sairam et al., 2011; Stewart et al., 2015; Cho et al., 2018; Hammal et al., 2020). The V_{Se} is computed according to Equation (1):

$$V_{Se} = \frac{d_0}{\sum_{i=1}^{n}(d_i/V_{Si})}, \tag{1}$$

where V_{Si} and d_i represent V_S and the thickness of the ith layer in the top 30 m, respectively, and d_0 is the depth of calculation (Editorial Board of Geological Engineering Handbook, 2018; Dobry et al., 2000).

According to the V_{Se} and the thickness of the sedimentary layer, the site can be divided into four classes (Table 3): I, II, III, and IV. Class I sites are mainly rock and tight gravel soil with good compactness. Class II sites are dominated by medium-dense and loose gravel and coarse and medium-dense sand. Class III sites are dominated by loose gravel, coarse sand, medium sand, dense sand, medium-fine sand, and silty sand. Class IV sites are dominated by silty soil, loose silt, silty sand, and newly deposited cohesive soil (Meng YS, 2010; Editorial Board of Geological Engineering Handbook, 2018).

We obtained V_{Se} by the weighted average of V_S within a depth of 30 m (Figure 11). According to the calculation results, the V_{Se} values of the three lines correspond to class III sites. The V_{Se} of L1, L2, and L3 are 195.39–248, 208.54–219.46, and 196.3–223.96 m/s, respectively. The overall V_{Se} in the study area exhibits a small

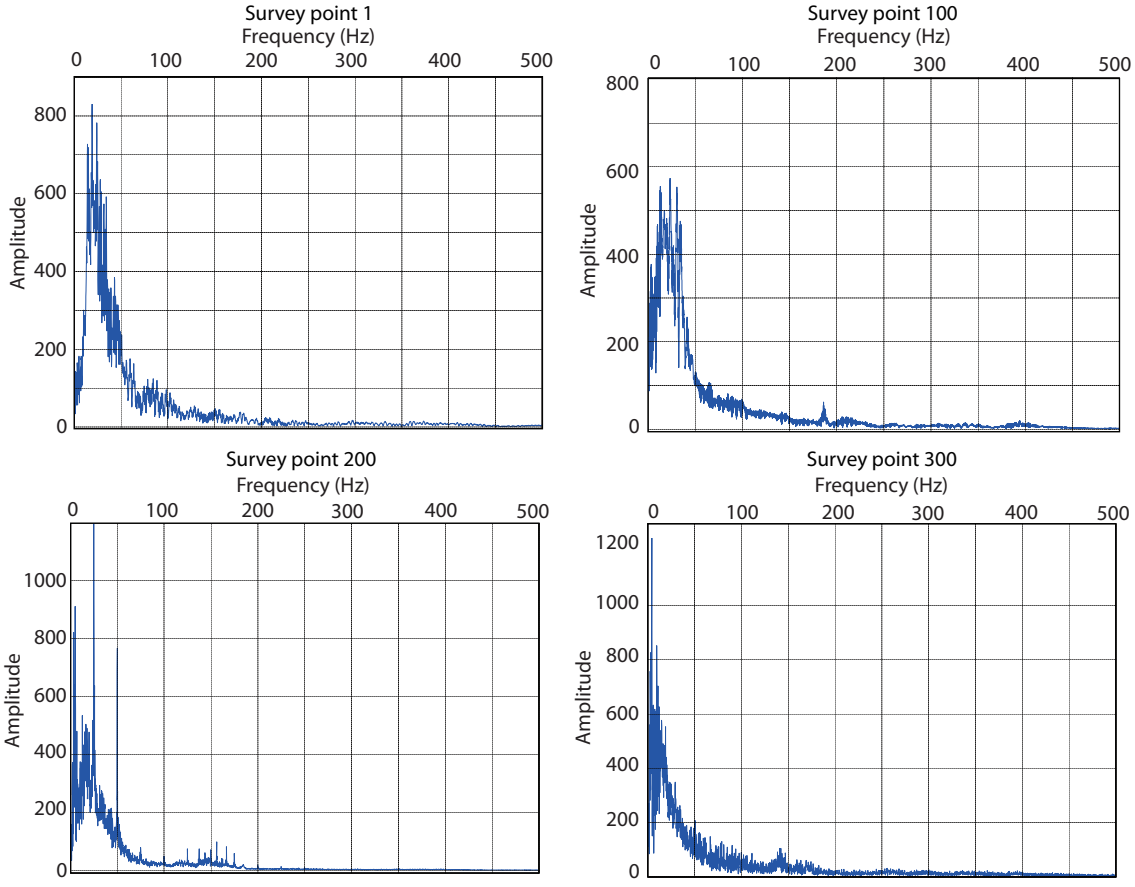

Figure 6. Frequency spectrum analysis (points 1, 100, 200, and 300 are surveying points with an equal interval spacing along line 1).

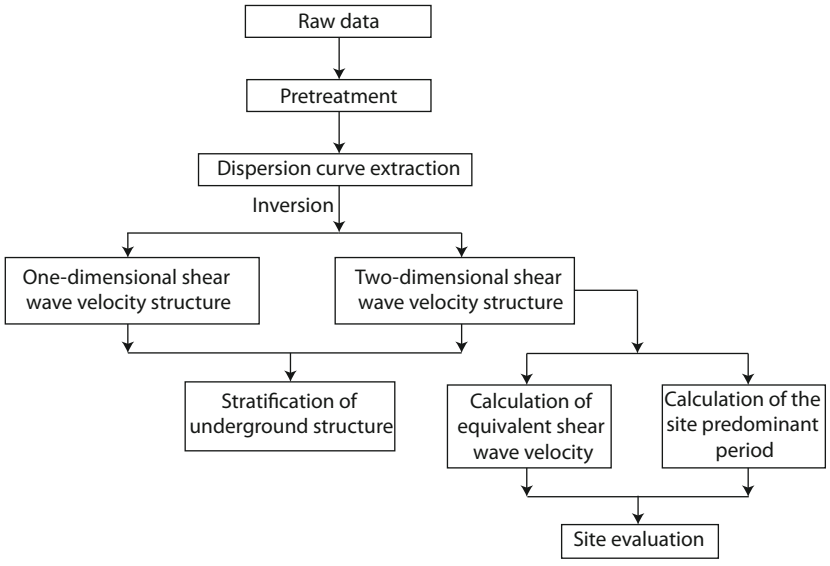

Figure 7. Surface wave data processing flowchart.

change, which is basically less than 250 m/s, within the velocity range of class III sites. Although L1 reaches 250 m/s locally, it corresponds to a class III site because the thickness of the overburden is greater than 50 m. The study area has good conditions for engineering geology and is suitable for the construction of basic engineering facilities.

4.2 Characteristics of the Predominant Period

Rock and soil are always highlighted with a certain period of wave selection amplification, and this period is referred to as the predominant period of the rock and soil. The period of the seismic wave is the same as the natural vibration period of the surface rock and soil, which will produce a resonance effect and seriously

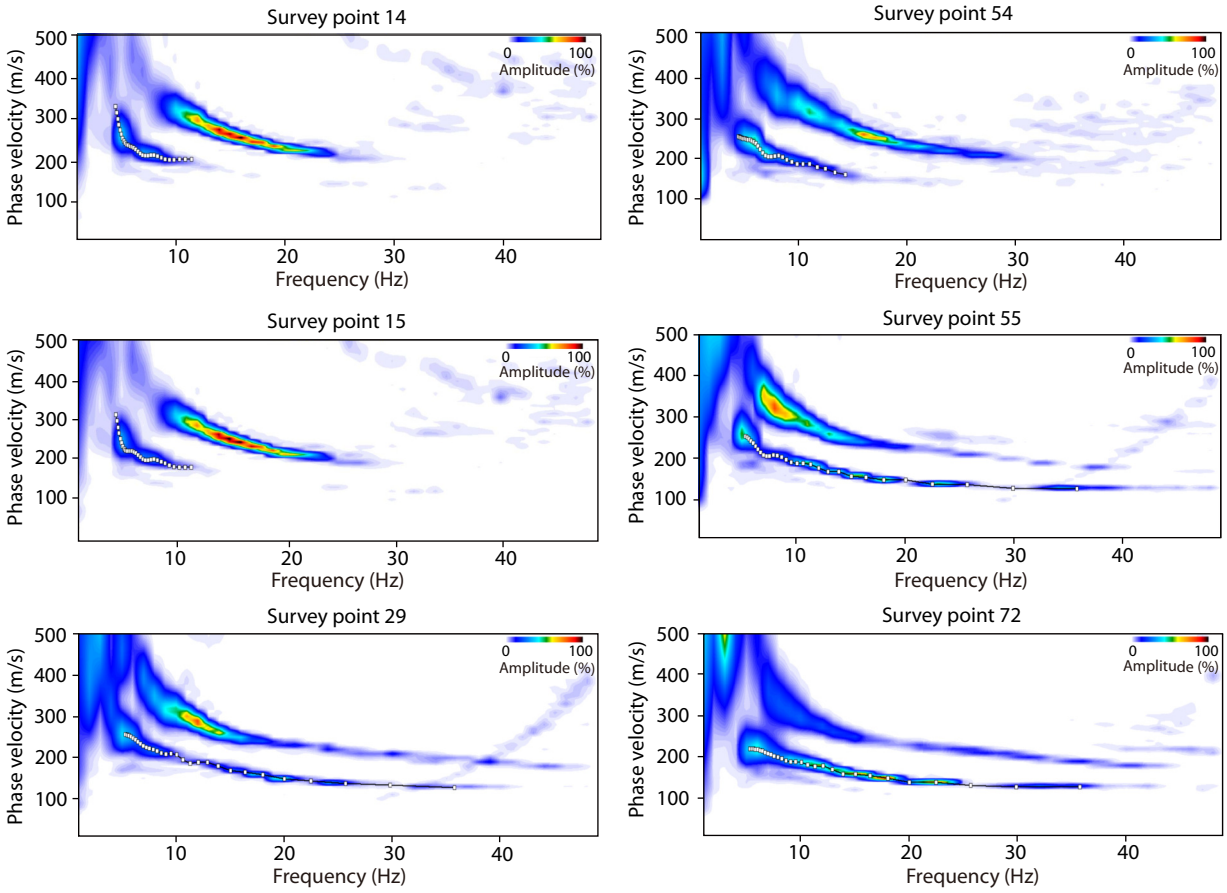

Figure 8. Dispersion curve extraction.

Table 2. Initial model parameter values.

Layer	Depth (m)	V_S (m/s)
First	1.47	146
Second	4.78	155
Third	8.53	276
Fourth	16.84	218
Fifth	26.4	420
Sixth	34.58	211
Seventh	Half-space	431

damage surface buildings (Editorial Board of Geological Engineering Handbook, 2018; Macau et al., 2018; Kim et al., 2019). Therefore, the impact of the predominant period of a site on the infrastructure is often considered in engineering design and construction. At present, the predominant period of a site can be calculated not only by experimental testing but also by calculating the V_S of the soil layer. Generally, the predominant period of a site should be calculated for the bedrock surface. If the bedrock surface is deep, it can be assumed to be 30–50 m. The predominant period of a site can be calculated according to Equation (2):

$$T = \sum_{i=1}^{n} \frac{4H_i}{V_{Si}}, \tag{2}$$

wherein T is the predominant period of the site, H_i is the thickness of the ith soil layer, and $V_{Si}$is the V_S of the ith soil layer (Sun XR et al., 2002; Zhang H et al., 2010).

The predominant periods of the three lines are shown in Figure 12. The maximum predominant periods of the L1, L2, and L3 survey lines are 0.776, 0.724, and 0.757 s, and the minimum values are 0.568, 0.648, and 0.63 s, respectively. Overall, the site period of excellence in the study area ranges from 0.568 to 0.776 s. According to the site classification in the code for seismic design of buildings, the site of the study area belongs to class III (Table 4). Therefore, according to the calculation results, in the overall structural design, the natural vibration period of the structure should be strictly controlled to avoid the predominant period of the site. For example, one should improve the damping performance of the embedded part of the structure, reduce the amplitude of the structure by increasing the buried depth of the building, conduct a foundation treatment to avoid the predominant period of the site, and adjust the overall stiffness of the building to avoid the predominant period of the site (Hao B et al., 2016).

5. Discussion

5.1 Stratification Characteristics

From the V_S profile (Figure 13a), we supposed that the layered effect of the underground structure within 40 m was obvious. The geological survey suggested that the soil layers in the study area are composed mainly of silt, clay, and silty sand and that the V_S is low. Previous geophysical explorations have found that five lithologic layers can be identified in the upper 50 m, including a silt

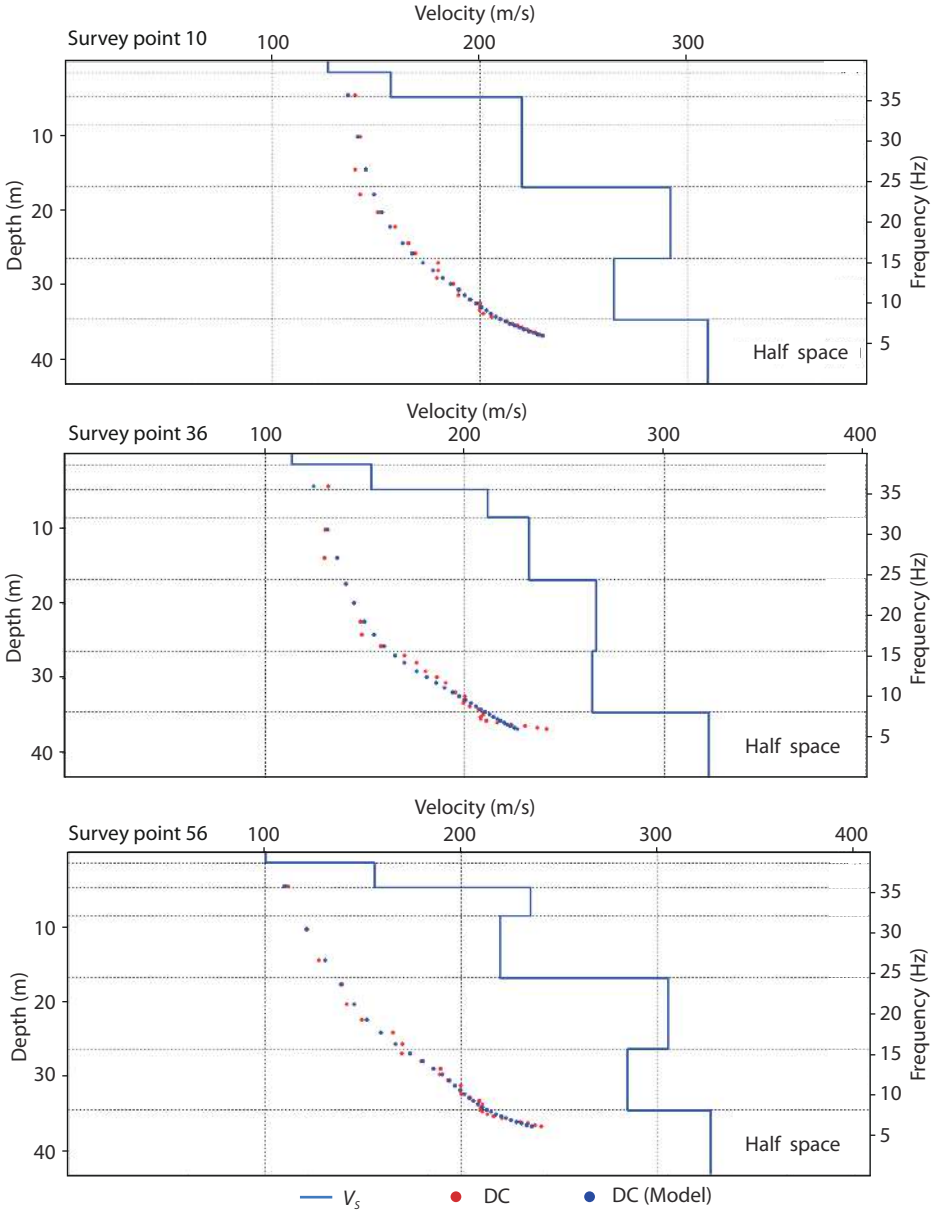

Figure 9. One-dimensional inversion (blue points: forward dispersion curve [DC (Model)]; red points: picked dispersion curve [DC]; blue line: shear wave velocity [V_S] layers).

Table 3. Classification of construction site soil (corresponding to different sedimentary layers).

V_{Se} (m/s)	Site category				
	I_0	I_1	II	III	IV
V_{Se} > 800 m/s	0	–	–	–	–
800 ≥ V_{Se} > 500 m/s	–	0	–	–	–
500 ≥ V_{Se} > 250 m/s	–	< 5	≥ 5	–	–
250 ≥ V_{Se} > 150 m/s	–	< 3	3 – 50	> 50	–
V_{Se} < 150 m/s	–	< 3	3 – 15	15 – 80	> 80

layer, a silty sand layer, a silty clay layer, an interbedded silty clay and fine sand layer, and a clay layer (Figure 13b; Ma Y et al., 2020). Therefore, we divided the V_S profile into five horizons according to the velocity differences. The 0–8 m layer is composed of anthropogenic miscellaneous fill, mainly exists in the shallow surface, and has a relatively small velocity change. The 8–14 m layer is discontinuous silty clay, and the V_S is relatively high. The 14–20 m layer is a silty sand layer, some of which contains water, so the V_S is markedly lower than that of silty clay. In the 20–30 m layer, the horizontal V_S changes greatly, and through comparison, we found that this layer is mainly silt. The V_S from 30–40 m is greater than 300 m/s. This layer is mainly a clay layer, and the velocity change is small.

5.2 Velocity Anomaly Analysis

In the V_S profiles, a low-velocity anomaly area is present from 20 to 40 m (Figure 13a, red box), and the speed range is basically between 100 and 200 m/s. We speculate that this may be the location of an ancient channel. In the Paleogene period, the region

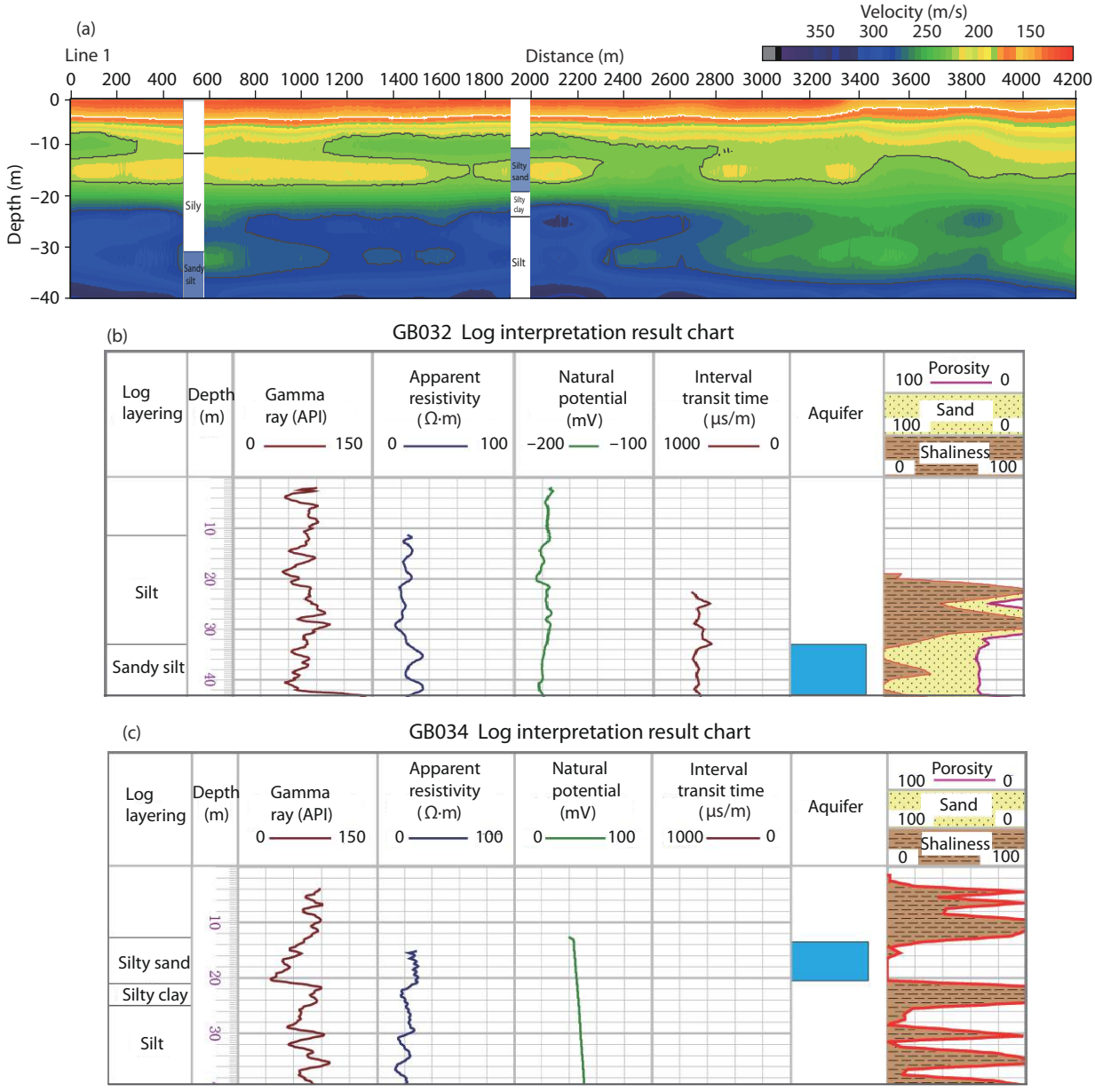

Figure 10. Comparative analysis of logging data for GB032 and GB034 (the two logging numbers along the survey line).

was characterized by high mountains and deep valleys and a hot, dry climate, and thick soil layers were deposited after many phases of subsidence. In the Neogene, the fluvial activity was further strengthened, and channel deposits with large thicknesses and wide areas formed. Previous researchers used the anti-interference electrical sounding method combined with logging data to identify the location of the ancient channel in this area (Zhang J et al., 2018). Therefore, we speculate, based on the geological data and previous research results, that several ancient riverbeds may be located within 40 m underground around Rongcheng County, some of which are close to the surface and some of which are deep. The V_S of these ancient channels is obviously low, and the layers are mainly silt.

5.3 Assessment of Engineering Geology Conditions

The study area is located at the periphery of the Rongcheng uplift in the Jizhong Depression, with a relatively flat terrain. The main stratum is silty sand, silt, and silty clay, with relatively better compactness and a high bearing capacity. A large amount of data shows that long-period buildings on weak sites and short-period buildings on hard sites are vulnerable to resonance damage during earthquakes. Therefore, the predominant periodic characteristics of the test site soil have important theoretical and practical significance in evaluating the foundation site and improving the seismic design of buildings. In the study area, the predominant period is characterized by an "overall low and local high." This value ranges from 0.568 to 0.776 s. According to the seismic fortification intensity of major cities in China, the seismic fortification intensity of Rongcheng County is 7°. In addition, it is categorized as class III according to the above-mentioned site categories. Therefore, the characteristic period value corresponds to 0.45 s (Table 5). The predominant periods of the sites in the study area are greater than this value, so this value satisfies the seismic fortification requirements.

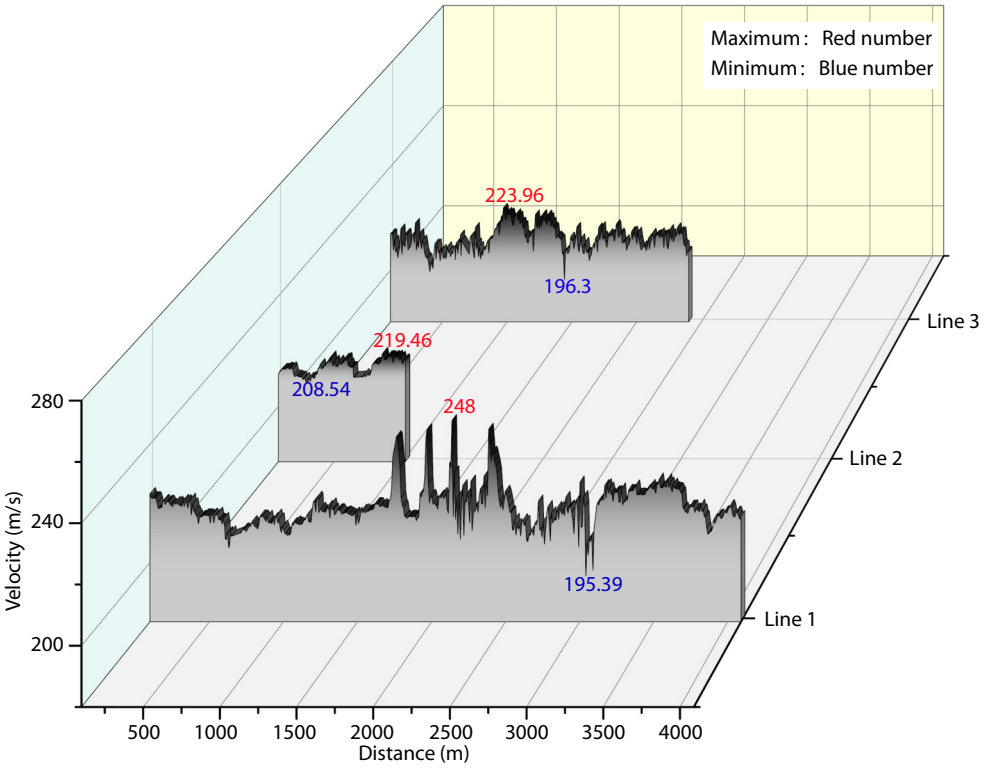

Figure 11. Equivalent shear wave velocity diagram.

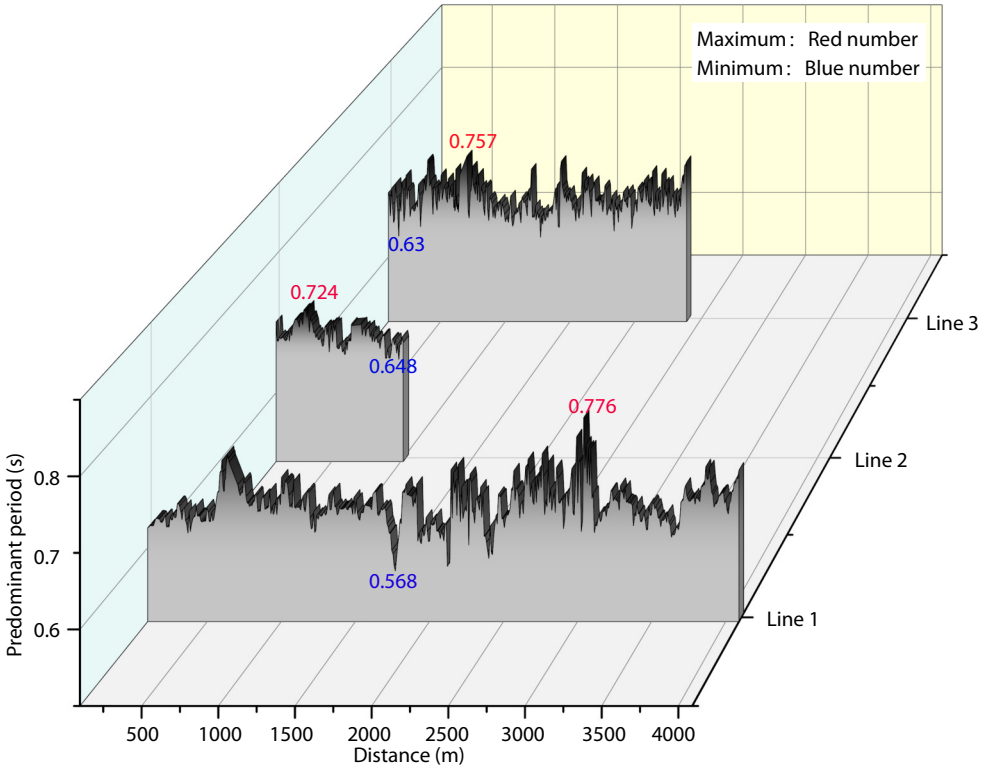

Figure 12. Predominant periods of line 1, line 2, and line 3.

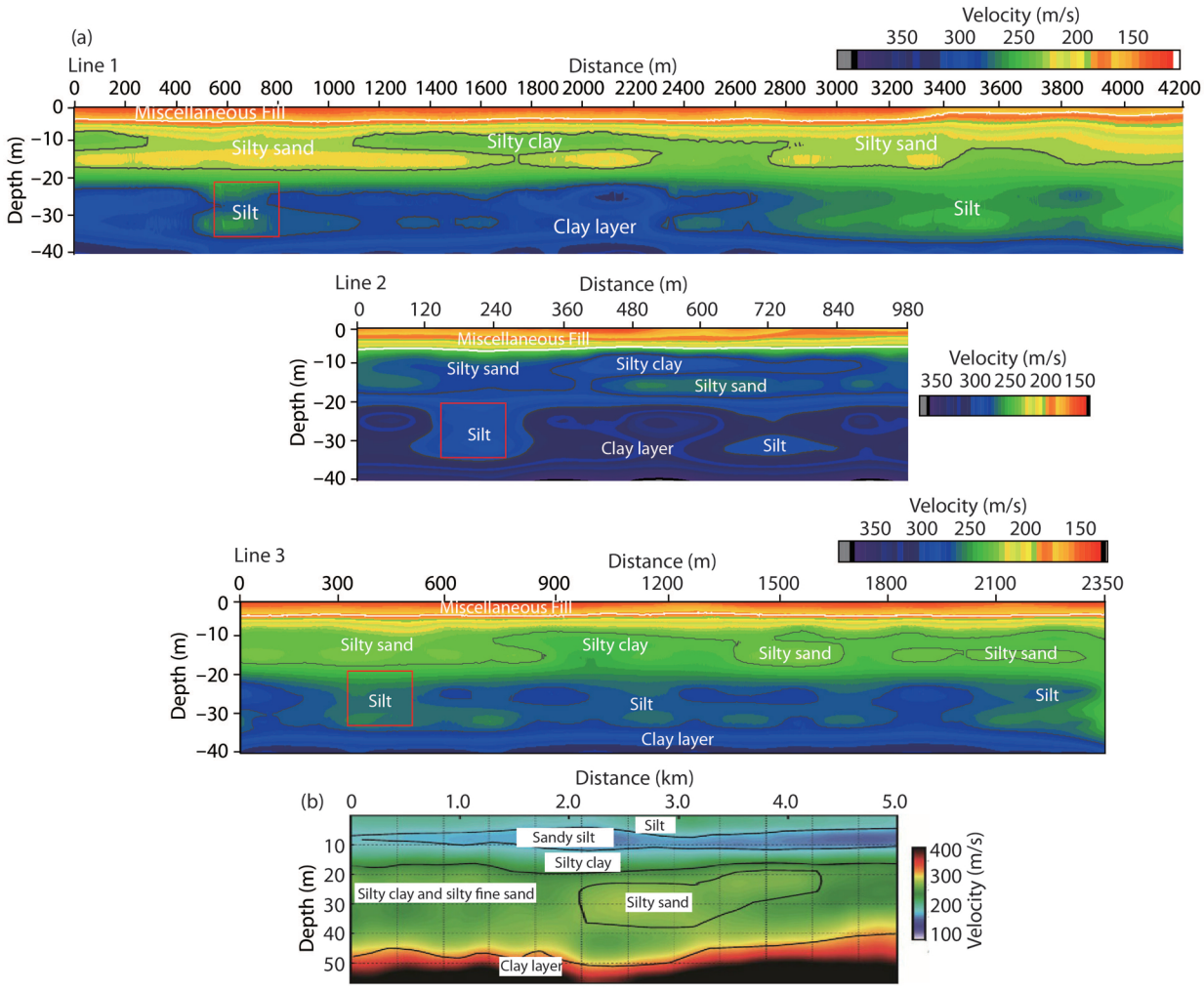

Figure 13. Interpretation of the stratigraphic structure (white line: miscellaneous soil layer; black line: structural layering of different soil layers; red box: inferred ancient channel location). (a) Underground structure layering diagram of the three different survey lines. (b) Structure modified from the work of Ma Y et al. (2020).

Table 4. Site classification according to the predominant period (Wang ZQ, 1994).

Site predominant period (T/s)	Site class
<0.1	I
0.1–0.4	II
0.4–0.8	III
>0.8	IV

Table 5. Design earthquake grouping and site categories (Zhang J et al., 2018).

Design earthquake grouping	Site category				
	I_0	I_1	II	III	IV
Group 1	0.20	0.25	0.35	0.45	0.65
Group 2	0.25	0.30	0.40	0.55	0.75
Group 3	0.30	0.35	0.45	0.65	0.90

6. Conclusions

On the basis of three near-surface active-source data sets from Rongcheng County, we obtained a high-precision near-surface velocity structure through the surface wave data processing method and interpreted it with drilling data. We used the V_S to calculate the predominant period and the V_{Se}, which is both time and labor saving compared with the traditional method. Finally, we reached the following two conclusions:

(1) Active-source surface wave exploration can be used to divide the structure of underground strata, study the positions of aquifers, and determine the depth of ancient channels. On the basis of the detection results, we divided 40 m of the subsurface in the study area into five layers, corresponding to anthropogenic miscellaneous fill, silty clay, silty sand, silty sediment, and clay. From the low-velocity anomaly area in the V_S profile, we concluded that the aquifer in the study area is mainly between 14 and 20 m and that the depth of the ancient channel is mainly between 20 and 30 m.

(2) In this study, the V_S was used to calculate the predominant period and the V_{Se} of the site. Compared with the traditional

method, this method is both time and labor saving. In the study area, the V_{Se} is basically within 220 m/s and belongs to a class III site. The predominant period of the site is between 0.56 and 0.77 s, so the underground foundation engineering of a construction project should avoid this predominant period range to prevent serious damage related to resonance.

Acknowledgments

We sincerely thank Li Qiusheng and Wang Zhihui from the Chinese Academy of Geological Sciences for their technical guidance in the process of writing this article. Han Rubing and Wu Qingyu from the Lithosphere Center of the Institute of Geology, Chinese Academy of Geosciences, provided considerable professional and technical support in the process of writing the paper and valuable suggestions during the establishment of the model. We express our sincere thanks to all the people who helped with this article. This study was supported by the National Natural Science Foundation of China (grant nos. 42074115, 41574094), the National Key R&D Program of China (grant no. 2017YFC0601301), the Geological Survey Project of the China Geological Survey (grant no. DD20189132), and the Key Laboratory of Deep-Earth Dynamics, Ministry of Natural Resources (grant no. J1901-3).

References

Aleardi, M., Salusti, A., and Pierini, S. (2020). Transdimensional and Hamiltonian Monte Carlo inversions of Rayleigh-wave dispersion curves: a comparison on synthetic datasets. *Near Surf. Geophys.*, *18*(5), 515–543. https://doi.org/10.1002/nsg.12100

Andajani, R. D., Ikeda, T., and Tsuji, T. (2019). Surface wave analysis for heterogeneous geological formations in geothermal fields: effect of wave propagation direction. *Explor. Geophys.*, *50*(3), 255–268. https://doi.org/10.1080/08123985.2019.1597497

Boore, D. M., Joyner, W. B., and Fumal, T. E. (1994). Estimation of response spectra and peak accelerations from western North American earthquakes: an interim report. Menlo Park, California: U.S. Geological Survey.

Cai, W., Song, X. H., Yuan, S. C., and Hu, Y. (2017). A new misfit function for multimode dispersion curve inversion of Rayleigh wave. *Earth Sci.* (*in Chinese*), *42*(9), 1608–1622. https://doi.org/10.3799/dqkx.2017.531

Cai, W., Song, X. H., Yuan, S. C., and Hu, Y. (2018). Fast and stable Rayleigh-wave dispersion-curve inversion based on particle swarm optimization. *Oil Geophys. Prospect.* (*in Chinese*), *53*(1), 25–34. https://doi.org/10.13810/j.cnki.issn.1000-7210.2018.01.004

Cao, L. H., Zuo, G. Q., Chen, C., and Shu, Z. P. (2012). The application of instant surface wave exploration to the survey of building foundation. *Chin. J. Eng. Geophys.* (*in Chinese*), *9*(2), 184–188. https://doi.org/10.3969/j.issn.1672-7940.2012.02.011

Cao, X., Xiong, Z. Q., and Zhang, D. Z. (2015). The Rayleigh surface wave intelligent inversion based on the BP artificial neural network. *Chin. J. Eng. Geophys.* (*in Chinese*), *12*(4), 514–519. https://doi.org/10.3969/j.issn.1672-7940.2015.04.017

Chimoto, K., and Yamanaka, H. (2019). S-wave velocity structure exploration of sedimentary layers using seismic interferometry on strong motion records. *Explor. Geophys.*, *50*(6), 625–633. https://doi.org/10.1080/08123985.2019.1654835

Cho, I., Urabe, A., Nakazawa, T., Sato, Y., and Sakata, K. (2018). Simple assessment of shallow velocity structures with small-scale microtremor arrays: interval-averaged S-wave velocities. *Explor. Geophys.*, *49*(6), 922–927. https://doi.org/10.1071/EG18020

Dal Moro, G., Pipan, M., and Gabrielli, P. (2007). Rayleigh wave dispersion curve inversion via genetic algorithms and marginal posterior probability density estimation. *J. Appl. Geophys.*, *61*(1), 39–55. https://doi.org/10.1016/j.jappgeo.2006.04.002

Dobry, R., Borcherdt, R. D., Crouse, C. B., Idriss, I. M., Joyner, W. B., Martin, G. R., Power, M. S., Rinne, E. E., and Seed, R. B. (2000). New site coefficients and site classification system used in recent building seismic code provisions. *Earthq. Spectra*, *16*(1), 41–67. https://doi.org/10.1193/1.1586082

Du, Z. T., Liu, L. M., and Cheng, D. W. (1999). The application of Rayleigh surface wave exploration technique to the quaternary stratification. *Geophys. Geochem. Explor.* (*in Chinese*), *23*(4), 277–282. https://doi.org/10.3969/j.issn.1000-8918.1999.04.006

Editorial Board of Geological Engineering Handbook. (2018). *Geological Engineering Handbook* (5th ed.) (in Chinese). Beijing: China Architecture & Building Press.

Fan, Y. L., Tan, C. X., Zhang, P., Sun, M. Q., Qi, B. S., Feng, C. J., Meng, J., and Wang, H. Q. (2020). A study of current in-situ stress state and its influence on tectonic stability in the Xiongan new area. *Acta Geosci. Sin.* (*in Chinese*), *41*(4), 481–491. https://doi.org/10.3975/cagsb.2020.040603

Fazelabdolabadi, B., and Golestan, M. H. (2020). Towards Bayesian quantification of permeability in micro-scale porous structures—the database of micro networks. *HighTech Innov. J.*, *1*(4), 148–160. https://doi.org/10.28991/HIJ-2020-01-04-02

Hammal, S., Bourahla, N., and Laouami, N. (2020). Neural-network based prediction of inelastic response spectra. *Civil Eng. J.*, *6*(6), 1124–1135. https://doi.org/10.28991/cej-2020-03091534

Han, B., Xia, Y. B., Pei, Y. D., Ma, Z., and Guo, X. (2020). Engineering geology characteristic and environmental geological effect of underground space in Xiongan New Area. *Geotech. Invest. Surv.* (*in Chinese*), *48*(3), 1–8.

Hao, A. B., Wu, A. M., Ma, Z., Liu, F. T., Xia, Y. B., Xie, H. L., Lin, L. J., Wang, T., Bai, Y. N., … Meng, Q. H. (2018). A study of engineering construction suitability integrated evaluation of surface–underground space in Xiongan new area. *Acta Geosci. Sin.* (*in Chinese*), *39*(5), 513–522. https://doi.org/10.3975/cagsb.2018.071502

Hao, B., Zhang, Y., Qiu, S. Y., and Hou, X. M. (2016). Calculation of site predominant period and its engineering application. *J. Water Resour. Arch. Eng.* (*in Chinese*), *14*(5), 144–150. https://doi.org/10.3969/j.issn.1672-1144.2016.05.028

He, P., Wang, Q. C., Wei, Y. L., and Liu, R. M. (2014). Study on quaternary sedimentary environment evolution of Raoyang sag in Central Hebei province. *Petrol. Geol. Eng.* (in Chinese), *28*(2), 24–26, 30. https://doi.org/10.3969/j.issn.1673-8217.2014.02.007

Hua, W. Y., Sun, B. X., and Xu, Y. (2002). Technology and application of transient surface wave method. *Heilongjiang Sci. Technol. Water Conserv.* (*in Chinese*), *30*(4), 106–107. https://doi.org/10.3969/j.issn.1007-7596.2002.04.063

Jin, C., Yang, W. H., Luo, D. G., and Liu, J. P. (2016). Comparative analysis of extracting methods of surface wave dispersion curves. *Progr. Geophys.* (*in Chinese*), *31*(6), 2735–2742. https://doi.org/10.6038/pg20160651

Kamel, F., and Badreddine, S. (2020). Liquefaction analysis using shear wave velocity. *Civil Eng. J.*, *6*(10), 1944–1955. https://doi.org/10.28991/cej-2020-03091594

Kim, J. K., Yoo, S. H., and Wee, S. H. (2019). Site amplification characteristics of bedrock using three reference site methods. *Explor. Geophys.*, *50*(4), 420–429. https://doi.org/10.1080/08123985.2019.1606203

Lei, T., Yao, H. J., and Zhang, C. (2020). Effect of lateral heterogeneity on 2-D Rayleigh wave ZH ratio sensitivity kernels based on the adjoint method: Synthetic and inversion examples. *Earth Planet. Phys.*, *4*(5), 513–522. https://doi.org/10.26464/epp2020050

Ma, F., Wang, G. L., Zhang, W., Zhu, X., Zhang, H. X., and Sun, Z. X. (2021). Influence mechanism of ancient buried hill geothermal development on land subsidence. *Geol. China* (*in Chinese*), *48*(1), 40–51. https://doi.org/10.12029/gc20210103

Ma, Y., Li, H. Q., Zhang, J., Sun, S., Xia, Y. B., Feng, J., Long, H., and Zhang, J. M. (2020). Geophysical technology for underground space exploration in Xiongan New Area. *Acta Geosci. Sin.* (*in Chinese*), *41*(4), 535–542. https://doi.org/10.3975/cagsb.2020.071001

Ma, Z., Xia, Y. B., Wang, X. D., Han, B., and Gao, Y. H. (2019). Integration of engineering geological investigation data and construction of a 3D geological structure model in the Xiong'an new area. *Geol. China* (*in Chinese*), *46*(S2), 123–138. https://doi.org/10.12029/gc2019Z213

Macau, A., Benjumea, B., Gabàs, A., Bellmunt, F., and Figueras, S. (2018). Geophysical measurements for site effects characterisation in the urban area of Girona, Spain. *Near Surf. Geophys.*, *16*(3), 340–355. https://doi.org/10.3997/1873-0604.2018004

Meng, Y. S. (2010). The regionalization and evaluation to engineering geologic of Handan based on tangential wave speed (in Chinese). Handan: Hebei University of Engineering. https://doi.org/10.7666/d.D587215

Pan, H., and Jiang, X. (2020). On the characteristics of ground motion and the improvement of the input mode of complex layered sites. *Civil Eng. J.*, *6*(5), 848–859. https://doi.org/10.28991/cej-2020-03091512

Park, C. B., Miller, R. D., Xia, J. H. (1999). Multichannel analysis of surface wave. *Geophysics*, *64*(3), 800–808. https://doi.org/10.1190/1.1444590

Pasquet, S., Bodet, L., Longuevergne, L., Dhemaied, A., Camerlynck, C., Rejiba, F., and Guérin, R. (2015). 2D characterization of near-surface V_P/V_S: surface-wave dispersion inversion versus refraction tomography. *Near Surf. Geophys.*, *13*(4), 315–331. https://doi.org/10.3997/1873-0604.2015028

Rastogi, B. K., Singh, A. P., Sairam, B., Jain, S. K., Kaneko, F., Segawa, S., and Matsuo, J. (2011). The possibility of site effects: the Anjar case, following past earthquakes in Gujarat, India. *Seismol. Res. Lett.*, *82*(1), 59–68. https://doi.org/10.1785/gssrl.82.1.59

Sairam, B., Rastogi, B. K., Aggarwal, S., Chauhan, M., and Bhonde, U. (2011). Seismic site characterization using V_{S30} and site amplification in Gandhinagar region, Gujarat, India. *Curr. Sci.*, *100*(5), 754–760.

Sairam, B., Singh, A. P., Patel, V., Chopra, S., and Kumar, M. R. (2019). V_{S30} mapping and site characterization in the seismically active intraplate region of Western India: implications for risk mitigation. *Near Surf. Geophys.*, *17*(5), 533–546. https://doi.org/10.1002/nsg.12066

Shang, S. J., Feng, C. J., Tan, C. X., Qi, B. S., Zhang, P., Meng, J., Wang, M. M., Sun, M. Q., Wan, J. W., … Xiang, X. X. (2019). Quaternary activity study of major buried faults near Xiongan New Area. *Acta Geosci. Sin.* (*in Chinese*), *40*(6), 836–846. https://doi.org/10.3975/cagsb.2019.033101

Song, Y. Y., Castagna, J. P., Black, R. A., and Knapp, R. W. (1989). Sensitivity of near-surface shear-wave velocity determination from Rayleigh and Love waves. *In* 1989 *SEG Annual Meeting* (*pp.* 509–512). *Dallas*, *Texas*, SEG. https://doi.org/10.1190/1.1889669

Stewart, J. P., Douglas, J., Javanbarg, M., Bozorgnia, Y., Abrahamson, N. A., Boore, D. M., Campbell, K. W., Delavaud, E., Erdik, M., and Stafford, P. J. (2015). Selection of ground motion prediction equations for the global earthquake model. *Earthq. Spectra*, *31*(1), 19–45. https://doi.org/10.1193/013013eqs017m

Sun, X. R., Liu, Z. G., Xu, D. E., and Dai, C. J. (2002). A study of shear wave for seismic stability evaluation of regional engineering sites in urban district of Shanghai. *Geophys. Geochem. Explor.* (*in Chinese*), *26*(5), 398–402. https://doi.org/10.3969/j.issn.1000-8918.2002.05.018

Shao, X. H., Yao, H. J., Liu, Y., Yang, H. F., Tian, B. F., and Fang, L. H. (2022). Shallow crustal velocity structures revealed by active source tomography and fault activities of the Mianning–Xichang segment of the Anninghe fault zone, Southwest China. *Earth Planet. Phys.*, *6*(2), 204–212. https://doi.org/10.26464/epp2022010

Wang, K., Zhang, J., Bai, D. W., Wu, X. G., Yue, H. Y., Zhang, B. W., Wang, X. J., and Zhang, K. (2021). Geothermal-geological model of Xiong'an New Area: evidence from geophysics. *Geol. China* (*in Chinese*), *48*(5), 1453–1468. https://doi.org/10.12029/gc20210511

Wang, Y. S., Yin, D. C., Wang, X. Q., Qi, X. F., Xia, Y. B., Ma, Z. T., Zhang, L., and Xu, R. Z. (2021). Groundwater–surface water interactions in the Baiyangdian wetland, Xiong'an New Area and its impact on reed land. *Geol. China* (*in Chinese*), *48*(5), 1368–1381. https://doi.org/10.12029/gc20210504

Wang, Z. Q. (1994). *A Manual for Siting in Earthquake Zones* (in Chinese). Beijing: China Architecture & Building Press.

Xia, J. H., Gao, L. L., Pan, Y. D., Shen, C., and Yin, X. F. (2015). New findings in high-frequency surface wave method. *Chin. J. Geophys.* (*in Chinese*), *58*(8), 2591–2605. https://doi.org/10.6038/cjg20150801

Yin, X. F., Xu, H. R., Xia, J. H., Sun, S. D., and Wang, P. (2018). A travel-time tomography method for improving horizontal resolution of high-frequency surface-wave exploration. *Chin. J. Geophys.* (*in Chinese*), *61*(6), 2380–2395. https://doi.org/10.6038/cjg2018L0373

Zhang, H., Cao, J., Gong, Y. L., and Li, Z. L. (2010). The application research of wave-velocity test technique in the evaluation of site earthquake resistant. *Comput. Tech. Geophys. Geochem. Explor.* (*in Chinese*), *32*(1), 68–72. https://doi.org/10.3969/j.issn.1001-1749.2010.01.013

Zhang, J., Ma, Z., Wu, A. M., Bai, Y. N., and Xia, Y. B. (2018). A study of paleochannels interpretation by the spectrum of lithology in Xiongan New Area. *Acta Geosci. Sin.* (*in Chinese*), *39*(5), 542–548. https://doi.org/10.3975/cagsb.2018.071003

Zhang, W., He, Z. Q., Hu, G., and Li, J. (2013). Detection of the shallow velocity structure with surface wave prospection method. *Progr. Geophys.* (*in Chinese*), *28*(4), 2199–2206. https://doi.org/10.6038/pg20130467